

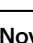


# Measuring the magnetic fields in the chromospheres of low-mass stars

Received: 23 November 2024

Accepted: 11 November 2025

Published online: 29 November 2025

 Check for updates

Tianqi Cang <sup>1,2</sup>, Pascal Petit <sup>3</sup>, Jean-François Donati<sup>3</sup>, Hui Tian <sup>4,5</sup>, Jianning Fu <sup>1,6</sup>, Hao Li<sup>5</sup>, Stefano Bellotti <sup>3,7</sup>, Xueying Hu <sup>1</sup>, Xiaoyu Ma<sup>1</sup>, Arturo Lopez Ariste<sup>3</sup>, Keyu Xing <sup>1</sup>, Julien Morin <sup>8</sup>, Hongpeng Lu<sup>9</sup> & Weikai Zong <sup>1,6</sup>

Magnetic fields in the upper atmospheres of solar-like stars are believed to provide an enormous amount of energy to power the hot coronae and drive large-scale eruptions that could impact the habitability of planetary systems around these stars. However, these magnetic fields have never been routinely measured on stars beyond the solar system. Through decade-long spectropolarimetric observations, we have now achieved the measurements of magnetic fields in the lower and middle chromospheres of three M-dwarfs. Our results indicate that the line-of-sight component of the chromospheric magnetic fields can reach up to hundreds of Gauss, whose sign frequently opposes that of the photospheric field. The measurements highlight the magnetic field complexity and the variation with height close to the surface of these M-dwarfs. They provide critical constraints on the energy budget responsible for heating and eruptions of stellar upper atmospheres, and enable assessments of how stellar magnetic activity may affect exoplanet environments.

As a layer of the stellar upper atmosphere, the chromosphere lies above the photosphere and beneath the corona<sup>1</sup>. It serves as the locus of thermal inversion, where the temperature begins to rise after decreasing from the stellar core to the photosphere. This characteristic demarcates it as more than a transitional layer, transforming it into a site with various types of activity<sup>2–5</sup>, which significantly influences the space weather conditions surrounding orbiting planets<sup>6,7</sup>. The magnetic field predominantly governs such activity, storing and releasing energy, thereby significantly affecting the heating processes and efficiently driving large-scale eruptions in the chromosphere and corona<sup>8</sup>. Consequently, measuring the magnetic field of the upper atmosphere, including the chromosphere, is essential to

understanding the physical mechanisms responsible for stellar coronal heating and eruptions<sup>9,10</sup>.

However, magnetic field measurements in the stellar upper atmosphere are very limited because of the weak signal, even for the Sun<sup>11–16</sup>. Although there have been attempts at magnetic field measurements in the chromospheres of accreting pre-main-sequence stars<sup>17,18</sup>, these signals are intertwined with the accretion process, which has a different energy-transfer mechanism compared to a solar-like chromosphere. In the absence of measurements, our knowledge about magnetic fields in the upper atmospheres of distant main-sequence stars other than the Sun relies on extrapolations<sup>19,20</sup> of the measured photospheric magnetic fields<sup>21,22</sup>. However, comparisons

<sup>1</sup>School of Physics and Astronomy, Beijing Normal University, Beijing, People's Republic of China. <sup>2</sup>Department of Scientific Research, Beijing Planetarium, Beijing, People's Republic of China. <sup>3</sup>Institut de Recherche en Astrophysique et Planétologie, Université de Toulouse, CNRS, IRAP/UMR 5277, Toulouse, France.

<sup>4</sup>School of Earth and Space Sciences, Peking University, Beijing, People's Republic of China. <sup>5</sup>State Key Laboratory of Solar Activity and Space Weather, National Space Science Center, Chinese Academy of Sciences, Beijing, People's Republic of China. <sup>6</sup>Institute for Frontiers in Astronomy and Astrophysics, Beijing Normal University, Beijing, People's Republic of China. <sup>7</sup>Leiden Observatory, Leiden University, Leiden, The Netherlands. <sup>8</sup>Laboratoire Univers et Particules de Montpellier, Université de Montpellier, CNRS, Montpellier, France. <sup>9</sup>State Key Laboratory of Public Big Data and Guizhou Radio Astronomical Observatory, Guizhou University, Guiyang, People's Republic of China. ✉ e-mail: [tianqi\\_cang@bnu.edu.cn](mailto:tianqi_cang@bnu.edu.cn); [ppetit@irap.omp.eu](mailto:ppetit@irap.omp.eu); [huitian@pku.edu.cn](mailto:huitian@pku.edu.cn); [jnfu@bnu.edu.cn](mailto:jnfu@bnu.edu.cn)

between the measured and extrapolated magnetic fields in the solar upper atmosphere often reveal distinct discrepancies, suggesting that the assumptions of extrapolations are invalid at many locations on stars<sup>4,13,23</sup>. Furthermore, the majority of magnetic energy in stellar atmospheres is stored in small-scale fields<sup>24,25</sup>, which are crucial for understanding stellar activity mechanisms. Unlike the photosphere, where magnetic structures are more concentrated, chromospheric fields typically exhibit more diffuse patterns<sup>26</sup>. Solar observations demonstrate that this structural complexity can lead to varying measurement outcomes across the chromosphere<sup>27</sup>, with magnetic field vectors sometimes appearing in opposite directions between chromospheric and photospheric layers in the same region<sup>28</sup>.

M-dwarfs are low-mass stars with surface temperatures lower than those of the Sun and extended convective envelopes. They are the most common type of star in the solar neighborhood, making up over 60% of all stars, and they host the majority of known exoplanets<sup>29</sup>. With a mass less than  $0.6M_{\odot}$ , M-dwarfs have a lifetime longer than that of the Sun, and the habitable zones of their orbiting exoplanets are closer, often less than 0.3 astronomical unit (AU) away from the stars<sup>30</sup>. The probability of detecting habitable planets is higher around M-dwarfs compared to earlier-type stars. However, the habitability is more likely to be influenced by the magnetic activity originating primarily from the host stars<sup>20,31,32</sup>. Many M-dwarfs exhibit greatly elevated levels of magnetic activity compared to our Sun, exhibiting frequent superflares with total energies of  $10^{33-38}$  erg<sup>33,34</sup>. While the surface magnetic fields of M-dwarfs have been measured over the past decades<sup>21,22,35</sup>, the energy driving this magnetic activity primarily originates from the magnetic fields in the upper atmospheres, which have not yet been measured<sup>36,37</sup>. In addition, many active M-dwarfs are fully convective stars, but it is still debated whether the lack of a tachocline will result in a dynamo different from the solar one. Understanding the key physical processes in these dynamos requires constraints from observations of small-scale magnetic field structures in stellar atmospheres, which are still lacking<sup>35</sup>.

Spectral lines originating at different atmospheric heights provide diagnostic windows into distinct stellar layers. While most absorption lines in stellar spectra form within the photosphere, the unique physical conditions in the chromosphere selectively enhance specific spectral features, particularly the Balmer lines and Calcium II lines. These enhanced emission features serve as valuable probes of chromospheric conditions and magnetic structures<sup>1</sup>. We analyzed a decade-long compilation of polarized spectra obtained with two high-resolution spectropolarimeters, ESPaDOnS and NARVAL (Methods). The data include the unpolarized normalized intensity (Stokes  $I$ , represented by normalization to the continuum  $I/I_c$ ) and circular polarization (Stokes  $V$ , represented by  $V/I_c$ ). This study focuses on three active mid to late M-dwarfs<sup>38</sup>: AD Leo, YZ CMi, and EV Lac, which have masses of 0.31–0.42 solar mass and rotation periods of 2.2–4.4 days (see Supplementary Information, SI hereafter, Table S1).

We simultaneously measured the mean longitudinal magnetic field (detailed in Method) of these stars in the photosphere ( $\langle B_p \rangle$ ) from mean photospheric lines, the lower chromosphere ( $\langle B_{cl} \rangle$ ) from the H $\alpha$  line, and the middle chromosphere ( $\langle B_{cm} \rangle$ ) from the cores of the Calcium II infrared triplet (Ca IRT). Figure 1 shows examples of Stokes  $I$  and  $V$  profiles for each star. The anti-symmetric features in the Stokes  $V$  profiles are typical signatures of the Zeeman effect<sup>39</sup>. Figure 2 presents all measurements for the three targets, along with the corresponding rotational phases of the observations<sup>40,41</sup>. The mean longitudinal magnetic fields in the chromospheres of the three targets can reach several hundred Gauss, comparable to the photospheric fields.

## Results

### Large-scale magnetic fields

The variation of the measured magnetic fields at different rotational phases can be used to characterize large-scale magnetic field

structures<sup>40,42</sup>. We typically obtained one spectrum per observation night for each star, resulting in low sampling coverage within one rotation cycle. Given that the large-scale photospheric magnetic field structure can vary yearly but generally remains stable within an observing epoch (the few-month window each year during which the targets are visible)<sup>43,44</sup>, we grouped the data by epochs for further analysis. The time duration of one epoch was at least one month, which is much longer than the stellar rotational period. Therefore, our measurements of the magnetic fields were taken over multiple rotation cycles within each epoch. For each target, we focus on measurements from a marked epoch with full rotational phase coverage: AD Leo observed in 2008, YZ CMi observed in late December 2007 and early 2008, and EV Lac in 2007. We neglect the effect of differential rotation, since it is not detected for the photospheric field in the three targets<sup>40</sup>. In these epochs, we see that observations at different times form relatively stable patterns in a phase-folded diagram, as shown in Fig. 2 (SI 1B & Fig. S3), which can be fitted by a two-harmonic Fourier series. This stability suggests that the large-scale chromospheric fields co-rotating with the stars were nearly stable within an epoch, with a timescale of at least one month.

### Layer-dependent magnetic fields

The different patterns of layers in the same epoch indicate that the large-scale magnetic fields vary with height. As shown in Fig. 2, while the sign of  $\langle B_{cl} \rangle$  is generally consistent with  $\langle B_p \rangle$ , frequent opposite signs in  $\langle B_{cm} \rangle$  highlight the different magnetic topologies with height. Among the three stars, AD Leo has the highest percentage of observations where  $\langle B_{cm} \rangle$  and  $\langle B_p \rangle$  have opposite signs. Example spectra with the opposite sign between photosphere and middle chromosphere can be found in Fig. 1 for AD Leo and EV Lac, showing the same orientation of the anti-symmetric structure for  $V$  profile and opposite orientation of  $I$  profile. Disk-integrated spectral profiles average the magnetic field contributions over the entire visible surface of the star, potentially masking localized mixed-polarity magnetic features but providing a comprehensive view of the star's overall magnetic structures. Considering that the chromospheric layer is close to the surface of a star (0.3%  $R_{\odot}$  for Sun), the variation in polarity and strength at different heights can be attributed to the variation of corresponding large-scale magnetic field structures with height, resulting in different contributions of positive- or negative-polarity fields to the observed signals. The sign change can be reproduced by extrapolation of the photospheric field (Fig. S4 & S5), but detailed variation between the patterns should be attributed to more complex effects close to the surface, like small-scale fields or more diffuse large-scale magnetic loops than predicted. This scenario is different from that on the Sun, where the polarity and topology of the magnetic field from the photosphere to the chromosphere are generally similar<sup>27,45</sup>.

### Complexity of magnetic structure

The correlation between the large-scale magnetic fields, as shown in Table 1 (more details in Table S2), can characterize the complexity of magnetic structure in the upper layers of the star during the marked epoch, or even considering the decade-long observations (see SI 1B and Figs. S6–S9). The difference between the large-scale fields is larger, as indicated by correlation coefficients approaching zero. YZ CMi displays distinct sinusoidal rotational modulation and exhibits the strongest correlation between photospheric and chromospheric fields among our observations, suggesting a more organized and stable magnetic field topology. The modulation patterns and correlations among different layers in the other two stars, EV Lac and AD Leo, exhibit more complex characteristics. In EV Lac,  $\langle B_{cl} \rangle$  also shows a substantial correlation with  $\langle B_p \rangle$ , similar to YZ CMi. However, there is a notable negative correlation between  $\langle B_{cm} \rangle$  and the fields in the lower layers. AD Leo exhibits weaker correlations between the layers; magnetic fields in both chromospheric layers appear to be anti-correlated

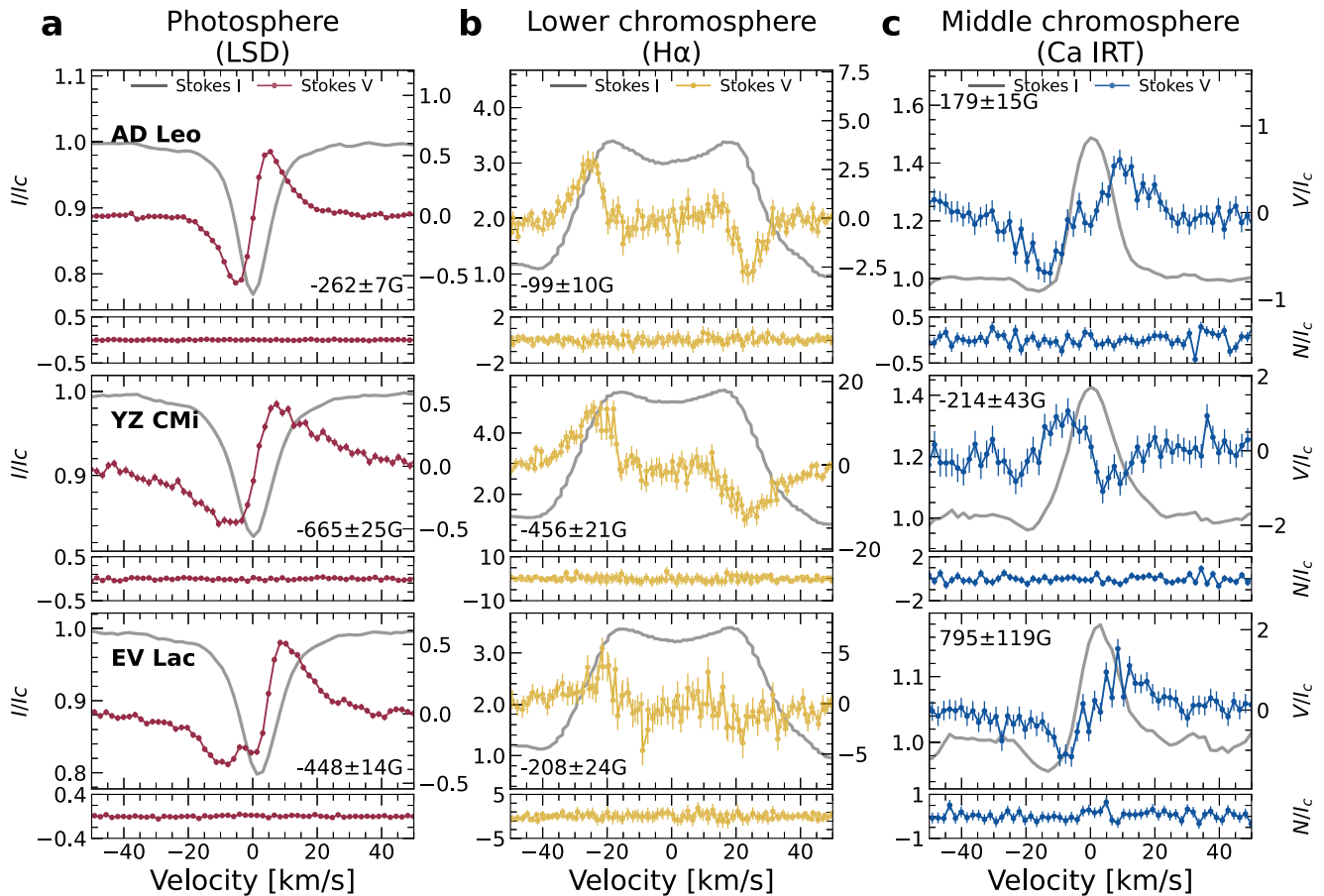


**Fig. 1 | Examples of spectropolarimetric spectral lines of three stars.** The profiles are sampled from the observations of 2007Jun25 (AD Leo), 2007Jan27 (YZ CMi), 2005Sep18 (EV Lac), with above-average signal-to-noise. **a** The spectral profiles of LSD line profile (photosphere). **b**  $H\alpha$  (lower chromosphere). **c** Ca IRT (middle chromosphere). The gray lines show the unpolarized intensity profiles normalized to the unpolarized continuum intensity  $I_c$ . The color lines represent

Stokes  $V$  profiles normalized to  $I_c$ , and the corresponding Null ( $N/I_c$ ) profile with no expected signal from the targets. Both  $V/I_c$  and  $N/I_c$  are multiplied by 100 for the purpose of illustration. The error bars of  $V/I_c$  indicate the  $\pm 1\sigma$  uncertainties. The velocities have been corrected from the stellar system radial velocity to shift the line center of photospheric LSD to 0 km/s. The inferred magnetic field is printed in each panel.

with the photospheric field during the marked epoch, while  $\langle B_{cl} \rangle$  and  $\langle B_{cm} \rangle$  are highly correlated. These observations suggest that YZ CMi has a more organized large-scale magnetic field structure than the other two stars (SI 1C). Previous theoretical investigations showed that more complex magnetic fields can support less prominence mass on M-dwarfs, resulting in weaker stellar winds<sup>19,46</sup>. AD Leo and YZ CMi are both believed to be fully convective stars with a strong dipole magnetic field<sup>43,47</sup>. Although the topologies are similar, YZ CMi has >30 times stronger stellar wind than AD Leo<sup>48</sup>. The difference in stellar winds from these M-dwarfs appears to be consistent with our evaluation of magnetic field complexity.

#### Relationship to flare occurrence and energetics

The occurrence frequency of solar flares has been found to be related to the complexity of magnetic field structures in active regions<sup>49</sup>. From observations of the Transiting Exoplanet Survey Satellite (TESS), we found that the flare frequency distributions on these stars likely relate to the complexity of the magnetic field (SI 1D and Fig. S10). The correlation analysis described above suggests that AD Leo has the most complex large-scale magnetic field among the three stars. We notice that, compared to the other two stars, AD Leo has fewer low-energy flares and more high-energy flares (especially superflares). The difference in stellar winds from these M-dwarfs appears to be consistent with our evaluation of magnetic field complexity. This suggests that

the occurrence frequency of superflares might be related to the complexity of large-scale magnetic fields on M-dwarfs. The potential explanation is that a richer small-scale field on the surface may produce a more complex field, which can lead to increased magnetic energy dissipation (thus more large flares and fewer small flares) and prune the flare frequency distribution.

#### Discussion

Our observations reveal stable large-scale magnetic fields in the lower and middle chromospheres of active M-dwarfs at a month-long timescale. The longitudinal magnetic fields at different atmospheric layers are generally correlated, which aligns well with those in solar observations<sup>27,45,50</sup>. Given the cancellation effect of opposite-polarity fields during disk integration, the average chromospheric fields could be as strong as the photospheric fields. The high magnetic field strengths we measured in the chromosphere, comparable to photospheric values, coupled with the complex structural variations identified across atmospheric layers, suggest that diffuse or even more complex magnetic field structures dominate the chromospheric topology of these active M-dwarfs. This finding aligns with observational evidence that these stars harbor abundant small-scale magnetic structures throughout their atmospheres<sup>25,35</sup>. This scenario also indicates that a substantial amount of magnetic energy is stored in the upper atmospheres of these stars, which may be released through

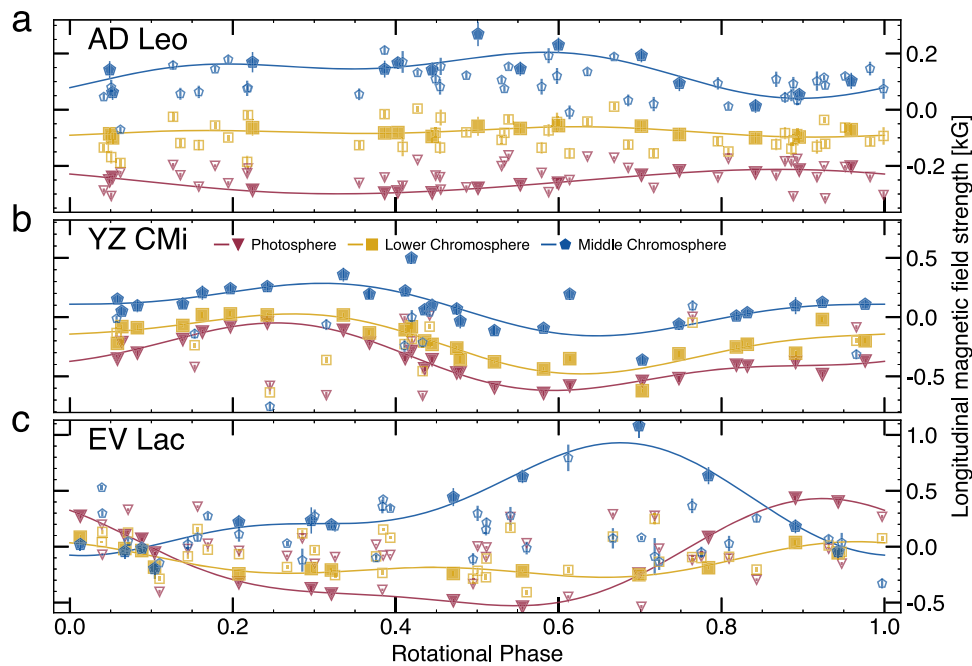


**Fig. 2 | Phase-folded mean longitudinal magnetic field strengths in the photospheres and chromospheres.** **a** AD Leo. **b** YZ CMi. **c** EV Lac. **a–c** The rotational phases were derived from the same ephemeris. Red triangles are photospheric fields ( $B_p$ ) inferred from LSD profiles; yellow squares are lower chromospheric fields ( $B_{cL}$ ) from H $\alpha$ , blue pentagons are middle chromospheric fields ( $B_{cM}$ ) from Ca

IRT. Filled markers are taken from a marked epoch with full phase coverage for each star. For these epochs, the linear Pearson correlation coefficients between the field strengths of two layers are also listed in the left block. For each marked epoch, we give a two-harmonic Fourier series to fit the pattern, showing the periodic signal of the magnetic field variation.

**Table 1 | Correlation coefficients ( $\rho$ ) of magnetic fields between layers (P for photosphere, cL and cM for lower and middle chromosphere)**

Star	$\rho_{(P,cL)}$		$\rho_{(P,cM)}$		$\rho_{(cL,cM)}$	
	Marked	All	Marked	All	Marked	All
AD Leo	-0.22	+0.26	-0.57	-0.19	+0.83	+0.64
YZ CMi	+0.84	+0.76	+0.65	+0.36	+0.79	+0.76
EV Lac	+0.84	+0.69	-0.45	-0.35	-0.57	-0.18

The coefficients are derived from all data, and a marked epoch with full phase coverage for each star.

flares, coronal mass ejections, and intense UV and X-ray radiation<sup>1,51</sup>. Such frequent eruptions and enhanced radiation likely have a large impact on the start and sustainability of life on nearby orbiting exoplanets<sup>32,52</sup>.

These findings provide critical constraints for understanding the energy budget responsible for heating and eruptions in the stellar upper atmospheres, thus enabling evaluation of the impact of various types of stellar magnetic activity on the habitability of surrounding exoplanets. Considering that chromospheric magnetic fields of stars other than the Sun have never been measured before, our study contributes observations that can inform investigations of magnetic fields in stellar upper atmospheres.

## Methods

### Spectropolarimetric observations

The Echelle SpectroPolarimetric Device for the Observation of Stars (ESPaDONs) is an instrument that includes an achromatic polarimeter. This device has been stationed at the Cassegrain focus of the 3.6 m

Canada-France-Hawaii Telescope at the top of Mauna Kea in Hawaii, USA, since early 2005<sup>53</sup>. Meanwhile, NARVAL (not an acronym) is a stellar spectropolarimeter that was designed based on ESPaDONs and was adapted to the specifics of the 2m T el escope Bernard Lyot (TBL), situated atop Pic du Midi in southwest France since 2006<sup>54</sup>. Under polarimetric mode, ESPaDONs and NARVAL provide complete coverage of the 370 to 1050 nm wavelength range and reach a resolution of  $R = 65,000$  in a single exposure. During this run, polarimetric exposures are divided into four consecutive subexposures. Each sub-exposure collects data at different angles of the two half-wave rotatable Fresnel rhombs in the polarimetric module. This sequence is designed to eliminate spurious polarization signatures at first-order<sup>55</sup>. In the standard procedures to extract the spectropolarimetric data, “Null” spectra are obtained by pair-processing sub-exposures corresponding to identical azimuths of the retarding plate or Cassegrain bonnette<sup>42</sup>, in parallel with polarized spectra. These “Null” spectra are not expected to contain any signal and should be pure noise if there is no spurious polarized signature in the  $V$  profile. We checked our  $V$  profile if any significant signal can be seen in the “Null” profile and whether it is similar to the  $V$  profile in order to exclude spurious signatures. The total efficiency of the instrument, including the spectrograph and CCD detector, is around 12%. The software package Libre-ESPRIT<sup>42,56</sup> is used for extracting the normalized, reduced data for unpolarized and polarized spectra corresponding to each observing sequence. All reduced spectra used in this work can be extracted from the PolarBase database<sup>57</sup>.

We only used the data from 2005-2019 observed with polarimetric mode, with the peak S/N of the Stokes  $V$  signal over 60. The basic stellar parameters of the selected M-dwarfs used in this work are taken from the study dedicated to their large-scale surface magnetic topologies<sup>40</sup>. The observation time is phased with the ephemeris:  $HJD = HJD_0 + P_{rot}E$ , where the zero point of heliocentric Julian dates is chosen equal to  $HJD_0 = 2,453,950.0$  and the rotational periods have been estimated from Zeeman-Doppler Imaging (ZDI) inversion<sup>40</sup>. Due

to the Earth's orbit, ground-based observations for our targets have only a few-month window per year, known as an epoch. A detailed observation log, including the information, can be found in Source Data.

### Magnetic fields measurement from the photosphere to the middle chromosphere

Using the Least Squares Deconvolution (LSD, detailed below) method<sup>42</sup>, we extracted average photospheric information from thousands of photospheric spectral lines and produced mean Stokes  $I$  and  $V$  profiles for all the unpolarized and polarized spectra, respectively. The longitudinal (line-of-sight projected) component of the stellar-disk integrated photospheric magnetic field ( $B_p$ ) was estimated from the first-order moment of the Stokes  $V$  profile based on the center-of-gravity (COG) method<sup>42,58</sup> described below. The cores of the Calcium II infrared triplet (Ca IRT) at wavelengths 849.8 nm, 854.2 nm, and 866.2 nm, typically formed in the middle chromosphere<sup>1,59</sup>, were analyzed. We applied the LSD method to these lines and subtracted the photospheric components to obtain the pure chromospheric Stokes  $I$  and  $V$  profiles (Fig. S1). The mean longitudinal magnetic field in the middle chromosphere ( $B_{cM}$ ) was estimated from these profiles using the COG method. Simultaneously, we measured the lower chromospheric longitudinal magnetic field ( $B_{cL}$ ) from the pure emitting hydrogen H $\alpha$  line at 656.3 nm (Details in SI 1A & Fig. S2)<sup>45,60</sup>.

### Mean line profiles derived by the Least-Squares Deconvolution method

Least-squares deconvolution (LSD) is a cross-correlation method, enabling the acquisition of average unpolarized and polarized line profiles with an improved signal-to-noise ratio. This enhancement uses spectral features formed in approximately the same disc region and height<sup>42</sup>. Line lists for photospheric analysis are generated from spectrum synthesis via model atmospheres extracted from the Vienna Atomic Line Database (VALD)<sup>61</sup>. We predominantly employed stronger lines corresponding to the photospheric absorption of an early-to-mid M spectral type star, aligning with the characteristics of our targets. Lines that deviate from the average behavior of the photosphere, particularly chromospheric emissions and telluric lines, are excluded from the list. Approximately 5000 intermediate to strong atomic absorption spectral lines are simultaneously utilized to extract the average polarization information in line profiles. This approach yields typical noise levels of about 0.06% (relative to the unpolarized continuum level) per 1.8 km/s velocity bin, resulting in a multiplex gain in Stokes  $V$  S/N of  $\sim 10$  for the photospheric mask. We applied the same approach to the three lines of Ca IRT and obtained an S/N gain of  $\sim 1.6$ . LSD is not applied to the H $\alpha$  line. We analyze H $\alpha$  individually since its broad Balmer wings break the LSD narrow-line approximation.

### Mean longitudinal magnetic field

In observations of these low-mass stars, we obtain only *disk-integrated* Stokes profiles. Consequently, the quantity we derive with the center-of-gravity (COG) technique is the longitudinal field,  $\langle B_\ell \rangle$ , i.e., the first moment of the circular polarization (Stokes  $V$ ) profile that represents the line-of-sight (LOS) integral over the visible stellar hemisphere. Because it is an LOS projection,  $\langle B_\ell \rangle$  can take positive or negative values depending on whether the net signed flux points toward or away from the observer; its magnitude should not be interpreted as the absolute field strength at a specific atmospheric height. COG method is applicable for both the spatially resolved and unresolved profiles, and  $\langle B_\ell \rangle$  can be obtained from the first moment of the normalized Stokes  $V$ <sup>39,42,58</sup>:

$$\langle B_\ell \rangle = -2.14 \times 10^{-11} \frac{\int v V(v) dv}{\lambda_0 g_{\text{eff}} c \int [I_c - I(v)] dv}, \quad (1)$$

where  $v$  is the velocity to the line center,  $\lambda_0$  is the wavelength of the spectral line,  $c$  is the speed of light, and  $g_{\text{eff}}$  is the effective Landé factor. Note that this formula works for a magnetic field (kilo-Gauss) that is even stronger than that in the case of the weak field approximation (WFA), which assumes that the Zeeman splitting is significantly smaller than the line's Doppler width. Under WFA, circular polarization signatures are proportional to  $\langle B_\ell \rangle$  in the first order and can have the same estimation of  $\langle B_\ell \rangle$  as the COG method for weak fields with a similar expression<sup>58</sup>. In a strong field, WFA breaks. However, the COG method is still valid. The corresponding uncertainty mainly results from the photon noise of Stokes  $I$  and  $V$  profiles. This formula is used to estimate the mean photospheric longitudinal field from the mean photospheric line profiles obtained using the LSD method, with typical  $g_{\text{eff}} = 1.24$  and  $\lambda_0 = 650$  nm. In the chromosphere, the COG method is still valid and can be applied to chromospheric spectral lines<sup>62</sup>. In our work, we take  $g_{\text{eff}} = 1$  and  $\lambda_0 = 656.28$  nm for the H $\alpha$  line. For the LSD profiles of Ca IRT formed in the middle chromosphere, we have typical values of  $g_{\text{eff}} = 0.968$  and  $\lambda_0 = 858.56$  nm, taking from the LSD process, and the  $g_{\text{eff}}$  of each line is taken from the VALD.

### Subtract the photospheric components from CaIRT line profiles

Information about the middle chromosphere is extracted from the Ca IRT. Both the Stokes  $I$  and  $V$  signals of these three lines can be contaminated by photospheric signals from the stellar disk<sup>17</sup>. Considering the weak signal and similar profile shapes of the triplet, we applied the LSD method to the Ca IRT and obtained the mean Ca IRT Stokes  $I$  and  $V$  profiles. Assuming the wing of the broad absorption band (slightly outside the emission core) anchors to the photosphere in unpolarized Stokes  $I$  profiles, we use a Lorentzian model to fit the photospheric component<sup>17</sup>. This component has a broad enough Doppler profile, where the Zeeman splitting is negligible, and WFA is applicable (see Methods: Mean longitudinal magnetic field). Under the first-order, the corresponding photospheric model in circular polarized Stokes  $V$  profile is a derivation of the Lorentzian model multiplied by a fixed coefficient of  $-4.67 \times 10^{-12} g_{\text{eff}} \langle B_p \rangle \lambda_0 c$ , where  $\langle B_p \rangle$  is the mean longitudinal photospheric field estimated from the LSD. Figure S1 shows an example for modeling the photospheric components in Stokes  $I$  &  $V$ . The residual profiles for both Stokes  $I$  &  $V$  are used to estimate the mean longitudinal middle chromospheric field ( $B_{cM}$ ). The emission core of Ca IRT should be purely from the chromosphere, and we measured its magnetic fields with the COG method.

### Data availability

Data from Fig. 2 and the observation journal are provided in Source Data. The original spectral data can be accessed through the PolarBase database<sup>57</sup> at <https://www.polarbase.ovgso.fr>. Source data are provided with this paper.

### Code availability

The codes used to generate Figs. 1 and 2 are available on CodeOcean<sup>63</sup>. Additionally, a Python package for performing Least Squares Deconvolution (LSD) on spectra is accessible at <https://github.com/folsomcp/LSDpy>, as a part of SpecpolFlow<sup>64</sup>.

### References

1. Linsky, J. L. Stellar model chromospheres and spectroscopic diagnostics. *Annu. Rev. Astron. Astrophys.* **55**, 159–211 (2017).
2. De Pontieu, B. et al. Chromospheric Alfvénic waves strong enough to power the solar wind. *Science* **318**, 1574 (2007).
3. Tian, H. et al. Prevalence of small-scale jets from the networks of the solar transition region and chromosphere. *Science* **346**, 1255711 (2014).
4. Carlsson, M., De Pontieu, B. & Hansteen, V. H. New view of the solar chromosphere. *Annu. Rev. Astron. Astrophys.* **57**, 189–226 (2019).

5. Yang, Z. et al. Observing the evolution of the Sun's global coronal magnetic field over 8 months. *Science* **386**, 76–82 (2024).
6. Luger, R. et al. A seven-planet resonant chain in TRAPPIST-1. *Nat. Astron.* **1**, 0129 (2017).
7. Liu, J. et al. Solar flare effects in the Earth's magnetosphere. *Nat. Phys.* **17**, 807–812 (2021).
8. Hansteen, V. et al. The unresolved fine structure resolved: IRIS observations of the solar transition region. *Science* **346**, 1255757 (2014).
9. Daley-Yates, S., Jardine, M. M. & Johnston, C. D. Heating and cooling in stellar coronae: coronal rain on a young Sun. *Month. Not. R. Astron. Soc.* **526**, 1646–1656 (2023).
10. Lagg, A., Lites, B., Harvey, J., Gosain, S. & Centeno, R. Measurements of photospheric and chromospheric magnetic fields. *Space Sci. Rev.* **210**, 37–76 (2017).
11. Solanki, S. K., Lagg, A., Woch, J., Krupp, N. & Collados, M. Three-dimensional magnetic field topology in a region of solar coronal heating. *Nature* **425**, 692–695 (2003).
12. Fleishman, G. D. et al. Decay of the coronal magnetic field can release sufficient energy to power a solar flare. *Science* **367**, 278–280 (2020).
13. Yang, Z. et al. Global maps of the magnetic field in the solar corona. *Science* **369**, 694–697 (2020).
14. Chen, B. et al. Measurement of magnetic field and relativistic electrons along a solar flare current sheet. *Nat. Astron.* **4**, 1140–1147 (2020).
15. Jess, D. B. et al. Solar coronal magnetic fields derived using seismology techniques applied to omnipresent sunspot waves. *Nat. Phys.* **12**, 179–185 (2016).
16. Yang, Z. et al. Mapping the magnetic field in the solar corona through magnetoseismology. *Sci. China Technol. Sci.* **63**, 2357–2368 (2020).
17. Donati, J. F. et al. Magnetic fields and accretion flows on the classical T Tauri star V2129 Oph. *Month. Not. R. Astron. Soc.* **380**, 1297–1312 (2007).
18. Donati, J. F. et al. Non-stationary dynamo and magnetospheric accretion processes of the classical T Tauri star V2129 Oph. *Month. Not. R. Astron. Soc.* **412**, 2454–2468 (2011).
19. Jardine, M. & Collier Cameron, A. Slingshot prominences: nature's wind gauges. *Month. Not. R. Astron. Soc.* **482**, 2853–2860 (2019).
20. Vidotto, A. A. The evolution of the solar wind. *Living Rev. Sol. Phys.* **18**, 3 (2021).
21. Donati, J. F. & Landstreet, J. D. Magnetic fields of nondegenerate stars. *Annu. Rev. Astron. Astrophys.* **47**, 333–370 (2009).
22. Reiners, A. Observations of cool-star magnetic fields. *Living Rev. Sol. Phys.* **9**, 1 (2012).
23. Wiegelmann, T., Lagg, A., Solanki, S. K., Inhester, B. & Woch, J. Comparing magnetic field extrapolations with measurements of magnetic loops. *Astron. Astrophys.* **433**, 701–705 (2005).
24. Schrijver, C. J. et al. Large-scale coronal heating by the small-scale magnetic field of the Sun. *Nature* **394**, 152–154 (1998).
25. Kochukhov, O., Hackman, T., Lehtinen, J. J. & Wehrhahn, A. Hidden magnetic fields of young suns. *Astron. Astrophys.* **635**, A142 (2020).
26. Wiegelmann, T., Thalmann, J. K. & Solanki, S. K. The magnetic field in the solar atmosphere. *Astron. Astrophys. Rev.* **22**, 78 (2014).
27. Ishikawa, R. et al. Mapping solar magnetic fields from the photosphere to the base of the corona. *Sci. Adv.* **7**, eabe8406 (2021).
28. Robustini, C., Esteban Pozuelo, S., Leenaarts, J. & de la Cruz Rodríguez, J. Chromospheric observations and magnetic configuration of a supergranular structure. *Astron. Astrophys.* **621**, A1 (2019).
29. Bonfils, X. et al. The HARPS search for southern extra-solar planets. XXXI. The M-dwarf sample. *Astron. Astrophys.* **549**, A109 (2013).
30. Chabrier, G. & Baraffe, I. Theory of low-mass stars and substellar objects. *Annu. Rev. Astron. Astrophys.* **38**, 337–377 (2000).
31. Vidotto, A. A., Fares, R., Jardine, M., Moutou, C. & Donati, J. F. On the environment surrounding close-in exoplanets. *Month. Not. R. Astron. Soc.* **449**, 4117–4130 (2015).
32. Linsky, J. *Host Stars and Their Effects on Exoplanet Atmospheres: An Introductory Overview*, vol. 955 of *Lecture Notes in Physics* (Springer International Publishing, 2019). <http://link.springer.com/10.1007/978-3-030-11452-7>.
33. Candelaresi, S., Hillier, A., Maehara, H., Brandenburg, A. & Shibata, K. Superflare occurrence and energies on G-, K-, and M-type dwarfs. *Astrophys. J.* **792**, 67 (2014).
34. Chen, H. et al. Detection of flare-induced plasma flows in the Corona of EV Lac with X-ray spectroscopy. *Astrophys. J.* **933**, 92 (2022).
35. Kochukhov, O. Magnetic fields of M dwarfs. *Astron. Astrophys. Rev.* **29**, 1 (2021).
36. Wright, N. J., Drake, J. J., Mamajek, E. E. & Henry, G. W. The stellar-activity-rotation relationship and the evolution of stellar dynamos. *Astrophys. J.* **743**, 48 (2011).
37. Reiners, A. et al. Magnetism, rotation, and nonthermal emission in cool stars. Average magnetic field measurements in 292 M dwarfs. *Astron. Astrophys.* **662**, A41 (2022).
38. Engle, S. G. Living with a Red Dwarf: X-Ray, UV, and Ca II activity-age relationships of M Dwarfs. *Astrophys. J.* **960**, 62 (2024).
39. Degl'Innocenti, E. L. & Landolfi, M. *Polarization in Spectral Lines*. No. v. 307 in *Astrophysics and Space Science Library* (Kluwer Academic Publishers, 2004).
40. Morin, J. et al. Large-scale magnetic topologies of mid M dwarfs. *Month. Not. R. Astron. Soc.* **390**, 567–581 (2008).
41. Morin, J. et al. The stable magnetic field of the fully convective star V374 Peg. *Month. Not. R. Astron. Soc.* **384**, 77–86 (2008).
42. Donati, J. F., Semel, M., Carter, B. D., Rees, D. E. & Collier Cameron, A. Spectropolarimetric observations of active stars. *Month. Not. R. Astron. Soc.* **291**, 658–682 (1997).
43. Bellotti, S. et al. Monitoring the large-scale magnetic field of AD Leo with SPIRou, ESPaDOnS, and Narval. Towards a magnetic polarity reversal? *Astron. Astrophys.* **676**, A56 (2023).
44. Bellotti, S. et al. Long-term monitoring of large-scale magnetic fields across optical and near-infrared domains with ESPaDOnS, Narval, and SPIRou. The cases of EV Lac, DS Leo, and CN Leo. *Astron. Astrophys.* **686**, A66 (2024).
45. Mathur, H., Nagaraju, K., Joshi, J. & de la Cruz Rodríguez, J. Do H $\alpha$  Stokes V profiles probe the chromospheric magnetic field? An observational perspective. *Astrophys. J.* **946**, 38 (2023).
46. Waugh, R. F. P., Jardine, M. M., Morin, J. & Donati, J. F. Slingshot prominences: a hidden mass loss mechanism. *Month. Not. R. Astronomical Soc.* **505**, 5104–5116 (2021).
47. Shulyak, D. et al. Strong dipole magnetic fields in fast rotating fully convective stars. *Nat. Astron.* **1**, 0184 (2017).
48. Wood, B. E. et al. New observational constraints on the winds of M dwarf Stars. *Astrophys. J.* **915**, 37 (2021).
49. Toriumi, S. & Wang, H. Flare-productive active regions. *Living Rev. Sol. Phys.* **16**, 3 (2019).
50. Stenflo, J. O. Solar magnetic fields as revealed by Stokes polarimetry. *Astron. Astrophys. Rev.* **21**, 66 (2013).
51. Hall, J. C. Stellar chromospheric activity. *Living Rev. Sol. Phys.* **5**, 2 (2008).
52. Airapetian, V. S., Gloer, A., Gronoff, G., Hébrard, E. & Danchi, W. Prebiotic chemistry and atmospheric warming of early Earth by an active young Sun. *Nat. Geosci.* **9**, 452–455 (2016).
53. Donati, J. F., Catala, C., Landstreet, J. D. & Petit, P. ESPaDOnS: The New Generation Stellar Spectro-Polarimeter. Performances and First Results. In Casini, R. & Lites, B. W. (eds.) *Solar Polarization 4*, vol. 358 of *Astronomical Society of the Pacific Conference Series*, 362 (2006).

54. Aurière, M. Stellar Polarimetry with NARVAL. In Arnaud, J. & Meunier, N. (eds.) *EAS Publications Series*, vol. 9 of *EAS Publications Series*, 105 (2003).
55. Semel, M., Donati, J. F. & Rees, D. E. Zeeman-Doppler imaging of active stars. III. Instrumental and technical considerations. *Astron. Astrophys.* **278**, 231–237 (1993).
56. Donati, J. F. et al. The surprising magnetic topology of  $\tau$  Sco: fossil remnant or dynamo output? *Month. Not. R. Astron. Soc.* **370**, 629–644 (2006).
57. Petit, P. et al. PolarBase: a database of high-resolution spectro-polarimetric stellar observations. *Publ. Astron. Soc. Pac.* **126**, 469 (2014).
58. Rees, D. E. & Semel, M. D. Line formation in an unresolved magnetic element: a test of the centre of gravity method. *Astron. Astrophys.* **74**, 1–5 (1979).
59. Hintz, D. et al. Modeling the chromosphere and transition region of planet-hosting Star GJ 436. *Astrophys. J.* **954**, 73 (2023).
60. Hintz, D. et al. The CARMENES search for exoplanets around M dwarfs. Chromospheric modeling of M 2–3 V stars with PHOENIX. *Astron. Astrophys.* **623**, A136 (2019).
61. Piskunov, N. E., Kupka, F., Ryabchikova, T. A., Weiss, W. W. & Jeffery, C. S. VALD: The Vienna Atomic Line Data Base. *Astron. Astrophys. Suppl. Ser.* **112**, 525 (1995).
62. Albert, K. et al. Intensity contrast of solar network and faculae close to the solar limb, observed from two vantage points. *Astron. Astrophys.* **678**, A163 (2023).
63. Cang, T. et al. Measuring the magnetic fields in the chromospheres of low-mass stars. *The Code Ocean* <https://doi.org/10.24433/CO.1452632.v4> (2025).
64. Folsom, C. P. et al. Specpolflow: a new software package for spectropolarimetry using Python. *J. Open Source Softw.* **10**, 7891 (2025).

## Acknowledgements

T.C. and JNF acknowledges the support from the National Natural Science Foundation of China (NSFC) through the grants 12090040/12090042/12427804. H.T. acknowledges the support of NSFC grants 12425301/12250006 and the New Cornerstone Science Foundation through the Explorer Prize. J-F.D. acknowledges funding from the European Research Council (ERC) under the H2020 research & innovation program (grant agreement 740651 NewWorlds). T.C. acknowledges funding from the support of the NSFC through grant 12503035, the LAMOST fellowship as a Youth Researcher, which is funded by the Special Funding for Advanced Users, budgeted and administered by the Center for Astronomical Mega-Science, Chinese Academy of Sciences (CAMS), and the China Postdoctoral Science Foundation (2023M730297). T.C. and W.Z. acknowledge funding from the support of the NSFC through grant 12273002. JNF is supported by the China Manned Space Program with grant no. CMS-CSST-2025-A013, and the Central Guidance for Local Science and Technology Development Fund under No. ZYYD2025QY27. H.L. acknowledges the support of the National Key R&D Program of China (2021YFA1600500/2021YFA1600503). HP.L. acknowledges funding from the support of NSFC through grant 12103004. S.B. acknowledges funding from the Dutch Research Council (NWO) under the project “Exo-space weather and contemporaneous signatures of star-planet interactions”

(with project number OCENW.M.22.215 of the research programme “Open Competition Domain Science- M”).

## Author contributions

TQ.C. analyzed the spectral data, identified the polarized chromospheric signal in M-dwarfs, and wrote the manuscript. P.P., J-F.D., H.T., and TQ.C. designed the methods of magnetic field analysis. TQ.C., P.P., J-F.D., A.L.A., and J.N.F. contributed to the initial interpretation of spectral lines. P.P., J-F.D., J.M., and S.B. contributed to the original collection of spectra and the analysis of the photospheric magnetic field and contributed to the manuscript writing. H.T. substantially contributed to the analysis and interpretation of the chromospheric magnetic field and assisted in writing the manuscript. H.L. and HP.L. contributed to the theoretical model of the chromosphere as a confirmation of the feasibility of the magnetic field analysis method and contributed to the manuscript writing. XY.M., XY.H., KY.X., and WK.Z. contributed to the correlation analysis and illustration of the magnetic fields.

## Competing interests

The authors declare no competing interests.

## Additional information

**Supplementary information** The online version contains supplementary material available at <https://doi.org/10.1038/s41467-025-66624-9>.

**Correspondence** and requests for materials should be addressed to Tianqi Cang, Pascal Petit, Hui Tian or Jianning Fu.

**Peer review information** *Nature Communications* thanks Dermott Mullan and the other anonymous reviewers for their contribution to the peer review of this work. A peer review file is available.

**Reprints and permissions information** is available at <http://www.nature.com/reprints>

**Publisher’s note** Springer Nature remains neutral with regard to jurisdictional claims in published maps and institutional affiliations.

**Open Access** This article is licensed under a Creative Commons Attribution-NonCommercial-NoDerivatives 4.0 International License, which permits any non-commercial use, sharing, distribution and reproduction in any medium or format, as long as you give appropriate credit to the original author(s) and the source, provide a link to the Creative Commons licence, and indicate if you modified the licensed material. You do not have permission under this licence to share adapted material derived from this article or parts of it. The images or other third party material in this article are included in the article’s Creative Commons licence, unless indicated otherwise in a credit line to the material. If material is not included in the article’s Creative Commons licence and your intended use is not permitted by statutory regulation or exceeds the permitted use, you will need to obtain permission directly from the copyright holder. To view a copy of this licence, visit <http://creativecommons.org/licenses/by-nc-nd/4.0/>.

© The Author(s) 2025